

UC Berkeley

UC Berkeley Previously Published Works

Title

Early aftershocks and afterslip surrounding the 2015 Mw 8.4 Illapel rupture

Permalink

<https://escholarship.org/uc/item/88c3k67v>

Authors

Huang, Hui
Xu, Wenbin
Meng, Lingsen
[et al.](#)

Publication Date

2017

DOI

10.1016/j.epsl.2016.09.055

Peer reviewed

Early aftershocks and afterslip surrounding the 2015 Mw 8.4 Illapel rupture

Author links open overlay panel [HuiHuang^a](#) [WenbinXu^{bc}](#) [LingsenMeng^a](#) [RolandBürgmann^a](#) [Juan CarlosBaez^d](#)
Show more

<https://doi.org/10.1016/j.epsl.2016.09.055> [Get rights and content](#)

Highlights

-

Missing early [aftershocks](#) and [repeaters](#) are recovered by the [matched-filter](#) method.

-

Differential southward and northward expansion of early aftershocks are observed.

-

Repeaters and [geodetic data](#) reveal afterslip around the Illapel mainshock rupture.

Abstract

On 16 September 2015, the Mw 8.4 Illapel earthquake ruptured a section of the subduction thrust on the west coast of central Chile. The mainshock was followed by numerous aftershocks including some normal-faulting events near the trench. We apply a template matching approach to improve the completeness of early aftershocks within one month of the mainshock. To constrain the distribution of afterslip, we utilize repeating earthquakes among the aftershocks and perform a joint slip inversion of postseismic GPS and InSAR data. The results show that the aftershock zone abruptly expands to the south ~ 14 h after the mainshock while growing relatively continuously to the north within the first day. The repeating earthquakes accompanying the early expansion suggest that aseismic afterslip on the subduction thrust surrounding the coseismic rupture is an important triggering mechanism of aftershocks in addition to stress transfer or poroelastic effects. An energetic earthquake sequence near the trench initiated with a M 4.6 event ~ 3.5 h after the mainshock, suggesting delayed triggering by the static or dynamic stress changes induced by the mainshock. The spatial distribution of repeating earthquakes and the geodetic-inverted afterslip are consistent and appear to wrap around the large coseismic slip patch. Both data sets suggest that the largest cumulative afterslip is located at $\sim 30.5^\circ\text{S}$ to the north of the mainshock

rupture zone. The estimated postseismic moment released in the first ~24 days of afterslip is equivalent to an earthquake of Mw 7.5. The afterslip illuminates the velocity strengthening sections of the plate interface that surround the mainshock rupture, consistent with plate coupling models inferred from interseismic GPS velocities.

- **Previous article in issue**
- **Next article in issue**

Keywords

2015 Mw 8.4 Illapel earthquake

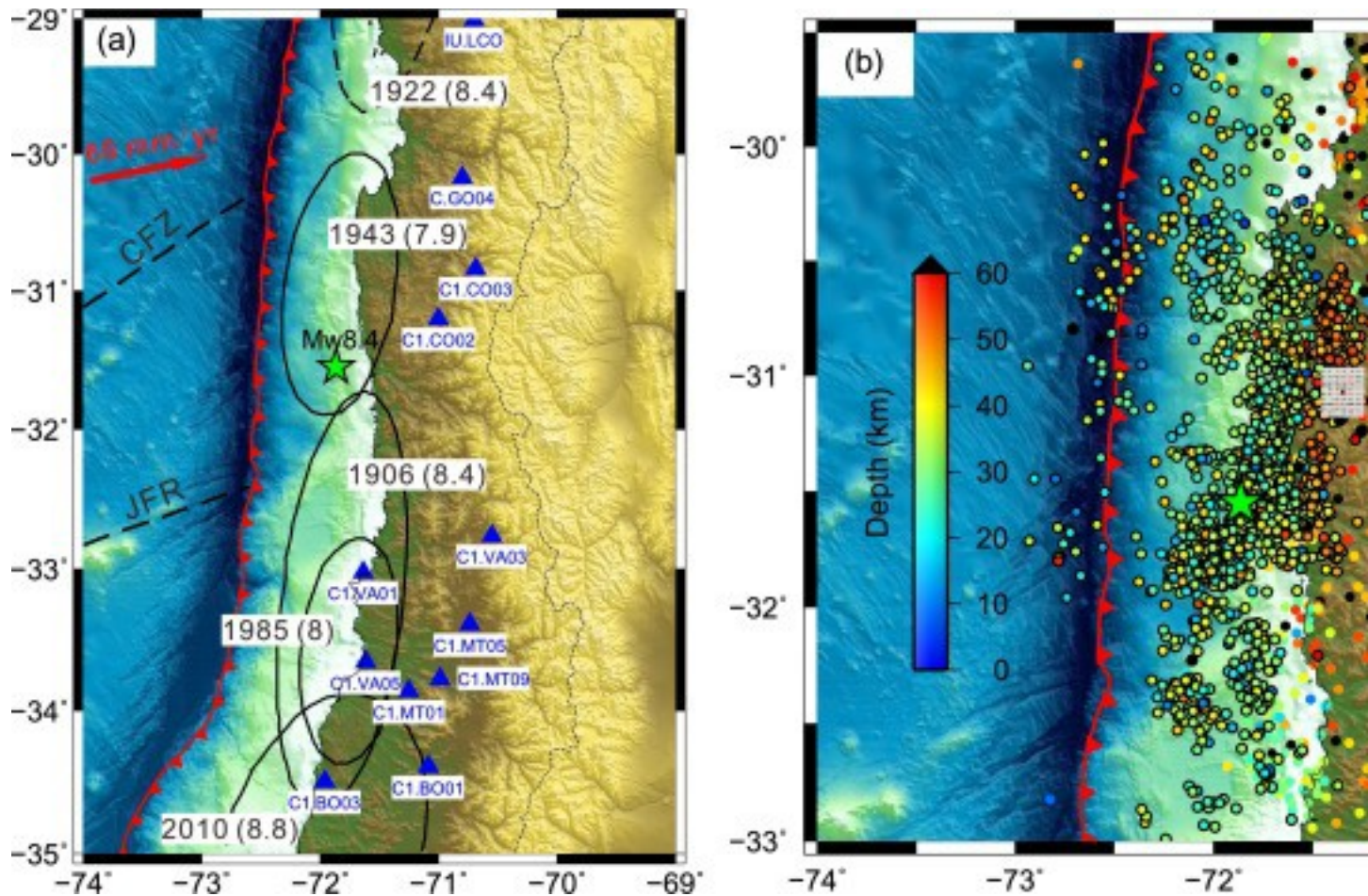
early aftershocks

repeating earthquakes

early afterslip

1. Introduction

The west coast of central Chile is characterized by the slightly oblique [subduction](#) of the [Nazca plate](#) underneath the South American plate, at a rate of ~68 mm/yr ([Fig. 1a](#), [Angermann et al., 1999](#), [Métois et al., 2012](#)). On 16 September 2015, the Mw 8.4 Illapel [earthquake](#) nucleated at 31.553°S, 71.864°W at a depth of 11.1 km, ~30 km offshore, according to the catalog determined by the Centro Sismológico Nacional (CSN; <http://www.sismologia.cl>). There are two major oceanic structures of the subducting Nazca plate around the 2015 Illapel event: the Challenger [Fracture Zone](#) (CFZ) and the Juan-Fernández Ridge (JFR). The JFR intersects the trench at ~32.5°S but the exact intersection of the CFZ with the trench remains unclear and high resolution multibeam [bathymetry](#) data do not clearly image the continuation of the fracture zone to the trench ([Fig. 1a](#), [Lange et al., 2016](#), [Yáñez et al., 2001](#)). The CFZ is associated with a crustal age offset of 3.5 Myr while the JFR represents a hot spot chain. Several large historical earthquakes occurred around the 2015 Illapel rupture zone, including the 1906 M 8.4 earthquake to the south and the 1922 M 8.4 earthquake to the north ([Fig. 1a](#)). Finite slip models and back-projection analyses of the Illapel event suggest that the rupture mainly extends to the north of the hypocenter (e.g., [Heidarzadeh et al., 2016](#), [Melgar et al., 2016](#), [Okuwaki et al., 2016](#), [Tilmann et al., 2016](#)). The [seismic energy](#) release of the earthquake was frequency dependent with a lower frequency section, corresponding to the area of greatest moment release, updip of a zone of strong high-frequency radiation ([Melgar et al., 2016](#), [Yin et al., 2016](#)).



1. [Download high-res image \(1MB\)](#)
2. [Download full-size image](#)

Fig. 1. (a) Map showing the 12 stations (blue triangles) used for [matched-filter](#) detection in this study. The black and dashed ellipses denote maximal rupture zones of instrumental and historical megathrust [earthquakes](#) ([Métois et al., 2012](#)). The green star denotes the [epicenter](#) of the 2015 Illapel M 8.4 mainshock. The two dashed lines indicate the Challenger [fracture zone](#) (CFZ) and Juan-Fernández Ridge (JFR). (b) The solid colored circles show the template locations color-coded by depth, with black dots denoting events with depth >60 km. The catalog is acquired from the Centro Sismológico Nacional, Universidad de Chile (CSN). The circles with outlines denote the [aftershocks](#) until 27 October 2015 while others denote events occurring from 1 January 2015 to the mainshock. The rectangular array of gray dots surrounding the template show an example of candidate grid locations used in matched-filter detection. (For interpretation of the references to color in this figure legend, the reader is referred to the web version of this article.)

The early [aftershocks](#) carry key information for understanding the mechanism of aftershock triggering processes, including the role of aseismic afterslip (e.g., [Meng et](#)

al., 2015, Peng and Zhao, 2009). According to the CSN catalog, the majority of early aftershocks occurred around the mainshock rupture with few events near the trench (Fig. 1b). However, due to the contamination by the mainshock coda and overlapping multiple phases, a large portion of early aftershocks may be undocumented in routine catalogs (Peng and Zhao, 2009). The [matched-filter](#) method is effective and widely used to recover uncataloged events before or after large earthquakes, which have been used to reveal the important role of aseismic slip in [foreshock](#) migration (e.g., Kato et al., 2012) and aftershock expansion (e.g., Lengliné et al., 2012) associated with the 2011 Tohoku earthquake.

Aseismic slip is an important fault behavior on [plate boundary](#) faults that contributes to the release of accumulated [strain](#) (e.g., Igarashi et al., 2003, Ozawa et al., 2011). The [kinematics](#) of secular aseismic slip on the plate interface can be effectively modeled by inversion of interseismic [GPS](#) velocities. Fault areas with high coupling are locked over the interseismic period while areas with weak coupling are partially releasing stress by aseismic sliding via steady fault creep, spontaneous slow slip events and postseismic afterslip. Métois et al. (2014) find that the plate coupling around the 2015 Illapel epicentral area (31°S–33°S) is very high (nearly 100%), whereas Tilmann et al. (2016) infer that the plate boundary slip deficit is relatively low between 31°S–32°S. An alternative method to measure the in-situ aseismic slip is by repeating earthquakes (e.g., Igarashi et al., 2003, Kato et al., 2012, Uchida and Matsuzawa, 2013). Repeating earthquakes are commonly interpreted as recurrent ruptures of [asperities](#) driven by surrounding aseismic slip (Nadeau and Johnson, 1998, Nadeau and McEvilly, 1999). While it can be challenging for geodetic postseismic models to separate the contributions from different postseismic relaxation processes (i.e., afterslip, viscoelastic relaxation and poroelastic rebound), in the portions of the megathrust where small asperities are available the repeating earthquakes directly image the [spatial distribution](#) and magnitude of aseismic afterslip (e.g., Uchida et al., 2004, Meng et al., 2015). On the other hand, geodetic measurements can constrain the aseismic slip where repeating earthquakes do not exist. Joint analysis of geodetic measurements and repeating earthquakes allows for much improved characterization of postseismic deformation and the determination of the contributing deformation processes (e.g., Shirzaei et al., 2013).

In this study, we investigate the spatio-temporal pattern of early aftershocks and afterslip of the 2015 Mw 8.4 Illapel earthquake. We perform template matching to obtain a more complete record of the aftershock sequence in the first month, which is further used to find repeating earthquakes that illuminate the area of slow slip following the

mainshock. We also use postseismic GPS and InSAR data to constrain the distribution of early afterslip following the mainshock. Finally we discuss the spatio-temporal pattern of the aftershock sequence and afterslip in comparison to the coseismic slip models and interseismic coupling models. The results shed light on the important role of aseismic slip in the early expansion of the aftershock zone and the release of stress on the partially coupled plate interface.

2. Matched-filter detection and repeating earthquake analysis

We first improve the early [aftershock](#) catalog by the [matched-filter](#) method (e.g., [Peng and Zhao, 2009](#), [Zhang and Wen, 2015](#)). We collect three-component broadband velocity [seismograms](#) (40-Hz sampling rate) at 12 stations ([Fig. 1a](#)) within 3 degrees from the mainshock [epicenter](#) (31.553°S, 71.864°W). We acquire continuous seismograms spanning from 16 September 2015 to 16 October 2015 from the Incorporated Research Institutions for [Seismology](#) (IRIS) [Data Management](#) Center (DMC). Most of the stations recorded data continuously during the study period ([Fig. S1](#)). The template catalog (1973 events, from 1 January 2015 to 27 October 2015, [Fig. 1b](#) and [Table S1](#)) is obtained from the CSN website (<http://www.sismologia.cl>). The template waveforms are windowed from 2 sec before to 6 sec after the theoretical S arrival time. The travel times are calculated based on a 1D velocity model used by the CSN for event location in the study region ([Ruiz et al., 2016](#)).

Both template and continuous waveforms are band-passed between 1 and 6 Hz with a fourth-order Butterworth filter. For a template to be analyzed, a minimum of 12 [channels](#) and a [signal-to-noise ratio](#) (SNR) greater than 5 are required. The SNR is estimated by comparing the template waveforms to a 8 sec time window ending 4 sec before the theoretical P arrival time. We compute the [cross-correlation](#) coefficient (CC) between the template waveforms and the corresponding continuous waveforms in a moving window with an increment of 0.025 s. The CC trace as a function of time is then averaged over all available channels. To better align the noncoherent CC traces induced by spatial separation of real events from the template, we shift the CC traces according to the theoretical S travel time difference between the grid location and the centered template before stacking ([Zhang and Wen, 2015](#)). Due to the poor depth sensitivity of [S wave](#) travel times, we only search the horizontal plane centered at each template with a grid of 0.2° by 0.2° and a spacing of 0.02° along both the latitude and longitude directions ([Fig. 1b](#)). The whole template dataset and their associated search grids cover a wide area around the mainshock, thus providing an excellent estimate of the locations

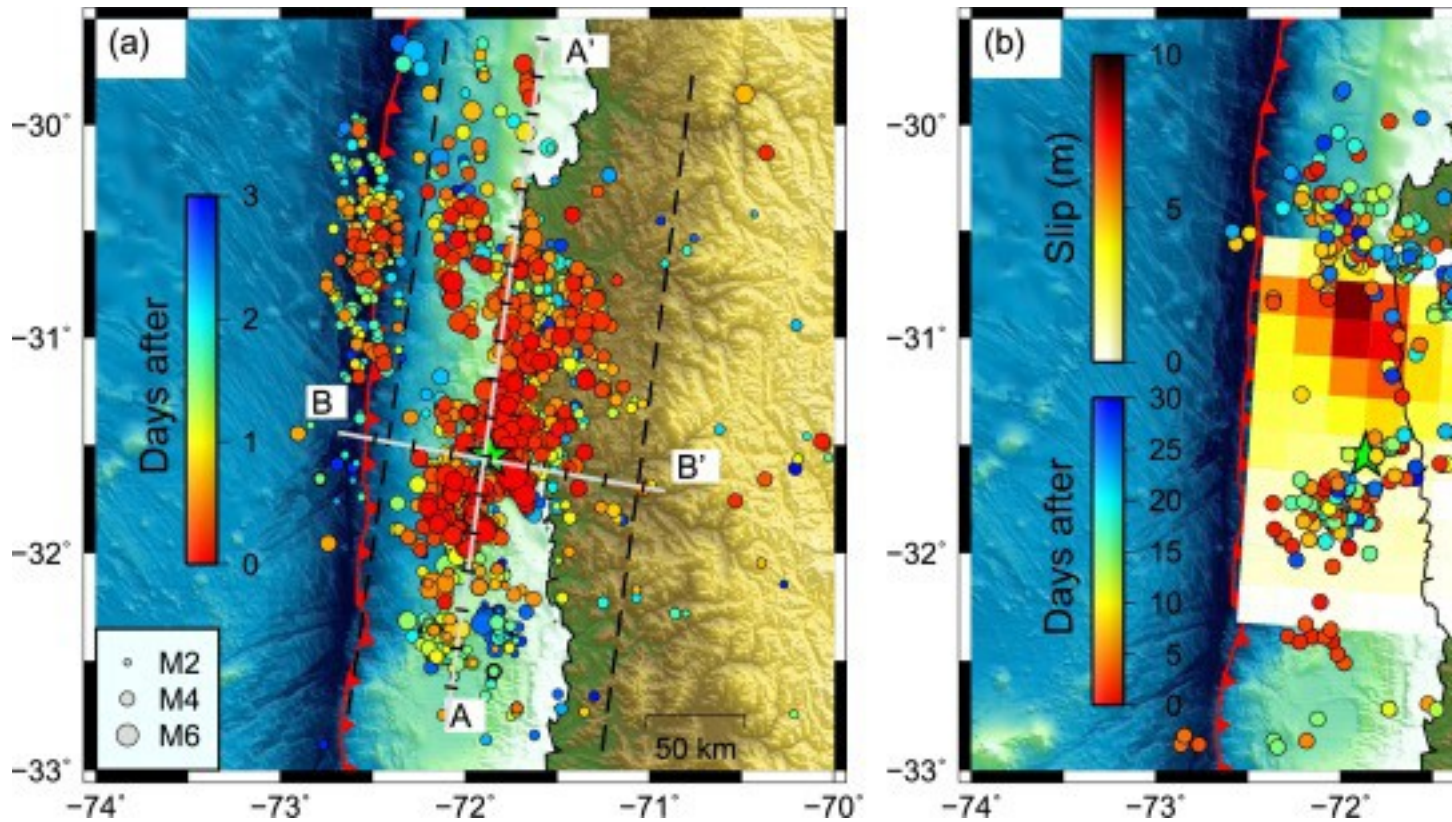
of detected events. The detection threshold is set at 11 times the median absolute deviation (MAD) of each daylong CC trace (e.g. Fig. S2), comparable to previous studies (e.g., [Peng and Zhao, 2009](#), [Kato et al., 2012](#)). To remove duplicate detections, if the same segment of continuous records (over 4 sec of overlap) is associated with multiple detections, only the template with highest mean CC is kept. Then the magnitude of each detected event is estimated according to the median value of the maximum amplitude ratios in all channels, assuming that one magnitude unit increase relative to the local magnitude in the template catalog corresponds to a tenfold amplitude increase ([Peng and Zhao, 2009](#)). A total of 7571 new events (including 7558 aftershocks) are detected from 16 September 2015 to 16 October 2015, ~5.4 times the number of events in the CSN catalog (1398 events) in the same time period.

Next we extract the repeating [earthquakes](#) from the new combined catalog ($M \geq 2.5$, from 1 January 2012 to 23 November 2015, Table S1). The analysis procedure is similar to previous studies (e.g., [Igarashi et al., 2003](#), [Uchida and Matsuzawa, 2013](#), [Meng et al., 2015](#)) and briefly described here. We convert the local magnitude (M_l) to moment magnitude (M_w) by using the same M_l – M_w relations as [Meng et al. \(2015\)](#). We only consider event pairs with hypocentral separations of less than 30 km and focal depths shallower than 80 km. The seismograms at 21 stations (Fig. S3) are acquired from the IRIS DMC. The vertical seismograms are bandpass filtered according to the source size: 1–4 Hz for event pairs with $M_w \geq 3$ or 1–8 Hz otherwise ([Igarashi et al., 2003](#), [Meng et al., 2015](#)). Waveforms are initially windowed from 3 s before the theoretical [P-wave](#) arrival times to 15 s after the S-wave arrival to include enough S wave energy. If the CC exceeds 0.95 and the magnitude difference estimated from the [logarithm](#) of the maximum amplitude ratio is smaller than 0.5 at two or more stations, the two events are classified as belonging to a group of repeating earthquakes (e.g., Fig. S4). Then all groups with common events are linked into the same [repeater](#) sequence.

A total of 291 sequences (712 events) of repeating earthquakes are identified. A large portion (~87%) of repeating earthquakes occur after the mainshock. There are 77 sequences that occur within a period of less than 7 days. Such isolated short-term sequences have been categorized as burst-type repeaters in previous studies ([Igarashi et al., 2003](#), [Templeton et al., 2008](#)). They may occur on [fault planes](#) within the overriding or the subducting plate and don't reflect creep on the [plate boundary](#) thrust ([Igarashi et al., 2003](#)).

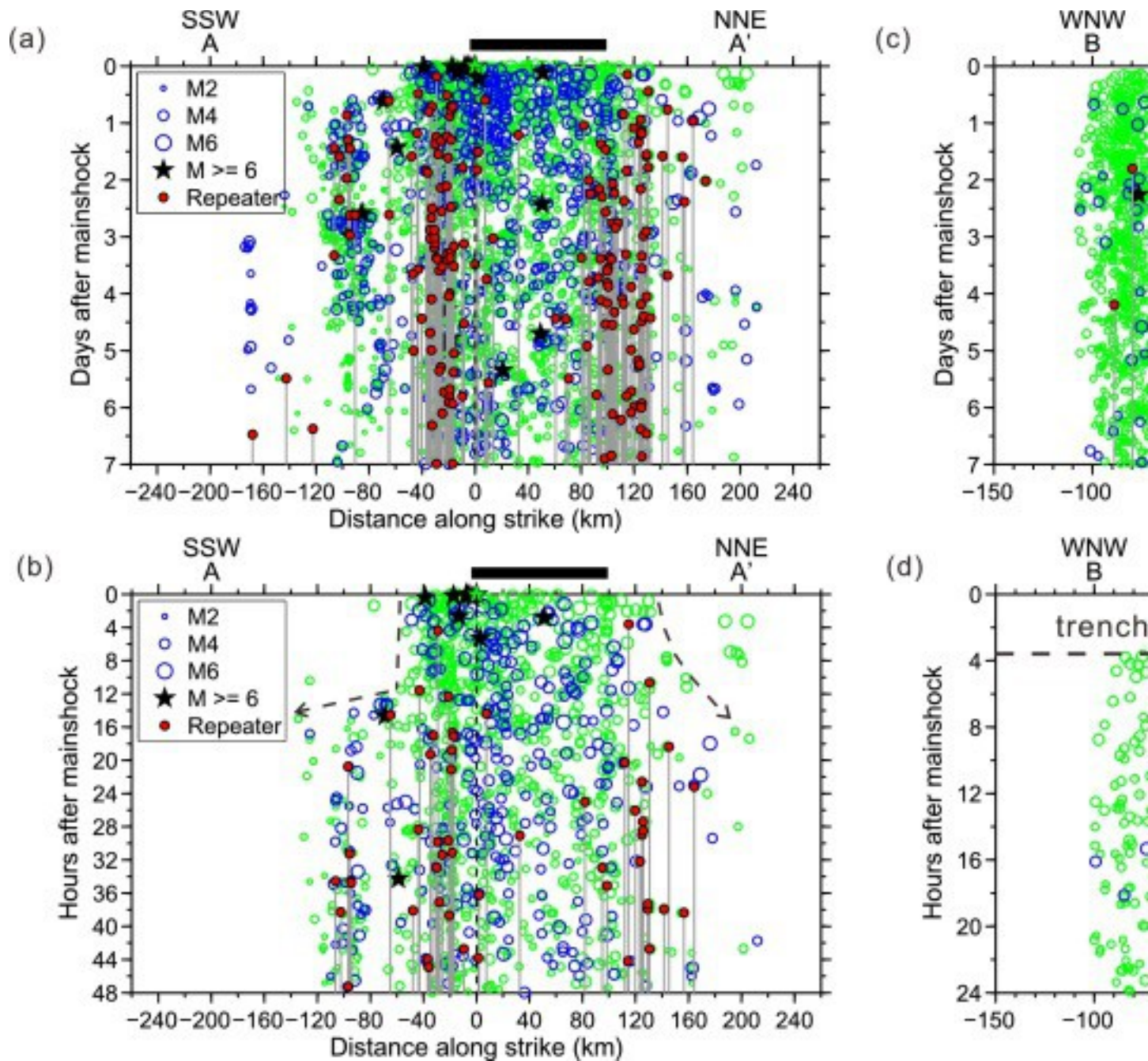
3. Spatio-temporal evolution of early aftershocks

[Fig. 2a](#) shows a map view of the first three days of [aftershocks](#), color-coded by the occurrence time since the mainshock. It shows that the early aftershocks migrate both northward and southward with time (symbol colors changing from red to blue). The triggered events close to the trench are mostly located at the northern side of the mainshock rupture. The repeating [earthquakes](#) found among the aftershocks in the first month are mainly distributed to the north, south and downdip of the large coseismic slip zone ([Fig. 2b](#)). Some [repeaters](#) are also identified among the near-trench events. [Fig. 3](#) shows the spatio-temporal evolution of early aftershocks and repeating earthquakes projected onto the along-strike profile AA' and along-dip profile BB' ([Fig. 2a](#)). In the along-strike direction, to exclude events near the trench, only the aftershocks between the dashed lines in [Fig. 2a](#) are plotted. The along-strike aftershock expansion is mainly seen within the first day after the mainshock. To the south of the rupture zone, the aftershocks within the first ~12 h contain several $M \geq 6$ events and repeaters and are confined within ~60 km distance from the mainshock [epicenter](#). At ~14 h after the mainshock there was a significant southward expansion to ~130 km, in contrast to the more steady southern aftershock expansion observed by [Lange et al. \(2016\)](#). In contrast to the south the northward expansion in the first day appears more continuous (from ~140 km to ~210 km) with no $M \geq 6$ events and fewer repeaters ([Figs. 3a and 3b](#)). The along-dip expansion is not clear within the first day after the mainshock ([Figs. 3c and 3d](#)). It is notable that the majority of repeating earthquakes wrap around the zone of large coseismic slip ([Figs. 2b and 3a](#)), in contrast to relatively more spatial overlap of the first 30-day aftershocks with the coseismic slip zone ([Fig. S5](#)). The area outside of the main coseismic slip zone includes many repeating groups recurring at short time intervals (connected with red lines), suggesting fast afterslip there.



1. [Download high-res image \(1MB\)](#)
2. [Download full-size image](#)

Fig. 2. (a) Map view of the combined dataset of newly detected events and the CSN catalog for first 3 days after the mainshock. The color denotes the differential origin time after the mainshock while the size scales with magnitude. The tick spacing on profiles AA' and BB' is 20 km. The black dashed lines indicate the western and eastern limits for [seismicity](#) used in along-strike projections ([Figs. 3a and 3b](#)). (b) Comparison of [repeater](#) activity within one month after the mainshock with the co-seismic model from [An and Meng \(2016\)](#).

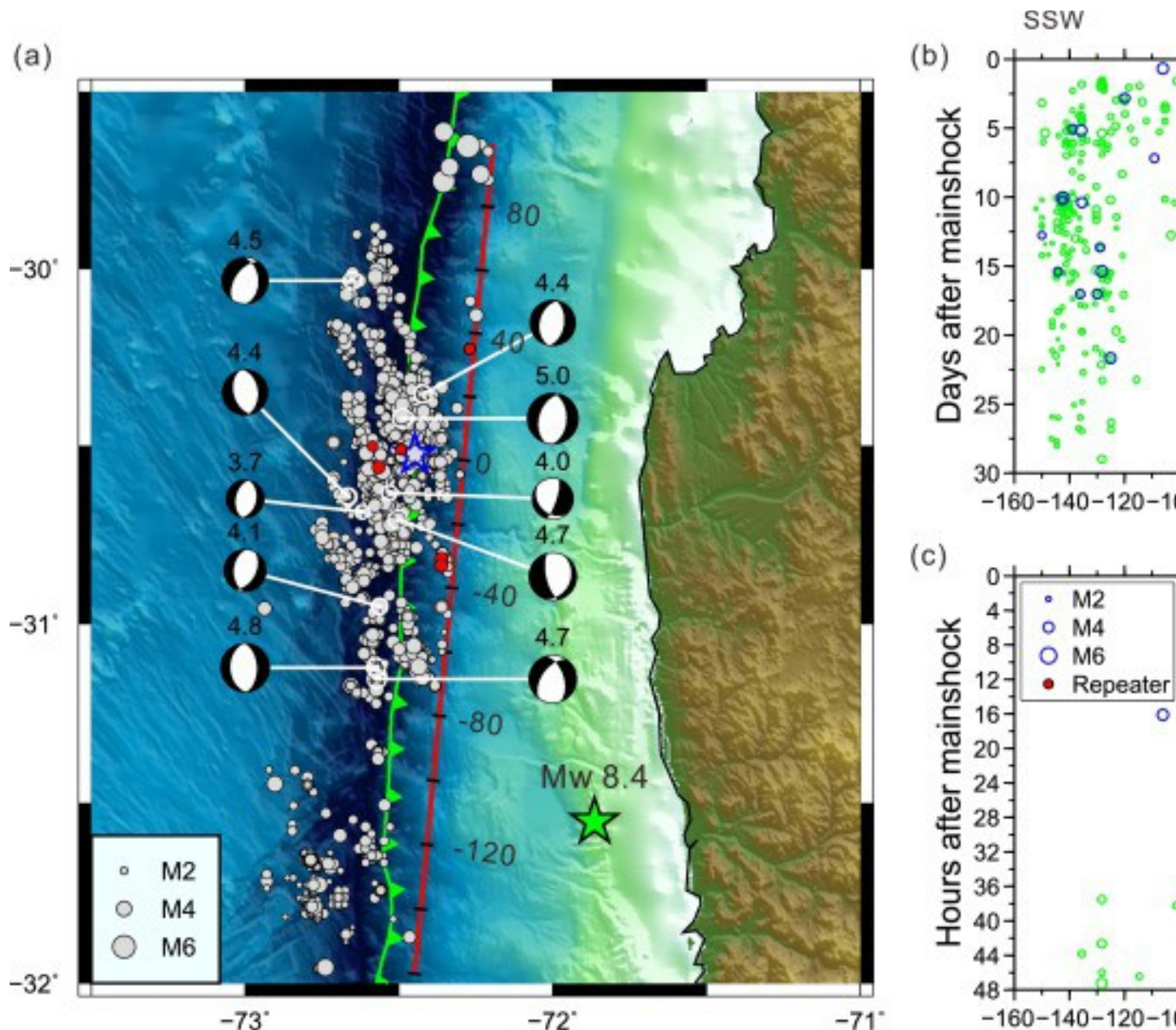


1. [Download high-res image \(2MB\)](#)
2. [Download full-size image](#)

Fig. 3. Migration of very early [aftershocks](#) within 7 days (a and c), 2 days (b) and 1 day after the mainshock (d). (a) and (b) show the along-strike distance of [seismicity](#) from between the black dashed lines ([Fig. 2a](#)) projected onto AA' with the mainshock [epicenter](#) at zero. The gray lines connect each repeating [earthquake](#) sequence, which are plotted at the average location. The two dashed lines depict the migratory patterns of aftershocks within the first day. (c) and (d)

show the along-dip distance projected onto BB'. See [Fig. 2](#) for the profile locations. The black bars on top of (a) and (b) show the extent of coseismic slip (larger than 20 percent of the maximum slip value of [An and Meng, 2016](#)'s model).

A lot of new events ($M \sim 0.9\text{--}4.6$) are detected near the trench in an elongated zone extending from $\sim 31^\circ\text{S}$ to 30°S (Figs. [2a](#), [3c](#) and [3d](#)). This earthquake sequence near the trench initiated with a $M 4.6$ event (30.52°S , 72.45°W , blue star in [Fig. 4a](#)), which is detected by the $M 5$ template with normal faulting mechanism reported by NEIC ([Fig. 4a](#)). Some other events also have normal faulting mechanisms as reported by NEIC or GEOFON, with the strike direction nearly parallel with the Chilean trench axis ([Fig. 4a](#)). It is notable that the whole sequence started ~ 3.5 h after the mainshock ([Fig. 3d](#)). The apparent time delay persists when lowering the detection threshold to 10 times the MAD or tightening to 15 times the MAD (Fig. S6), indicating a delayed response to the stress change induced by the mainshock in this area. Among these events, there are 10 repeaters (5 doublets, [Figs. 4a and 4b](#)). Two doublets have recurrence times smaller than 3 days while the other three doublets recur within 7–20 days, suggesting there may have been some triggered short-term fault creep in that area. In the first several hours, the [seismicity](#) appears to migrate northward along the trench axis from the location of the first $M 4.6$ event ([Figs. 4b and 4c](#)). This migratory pattern can still be observed when the threshold is increased to 15 times the MAD (Fig. S7).



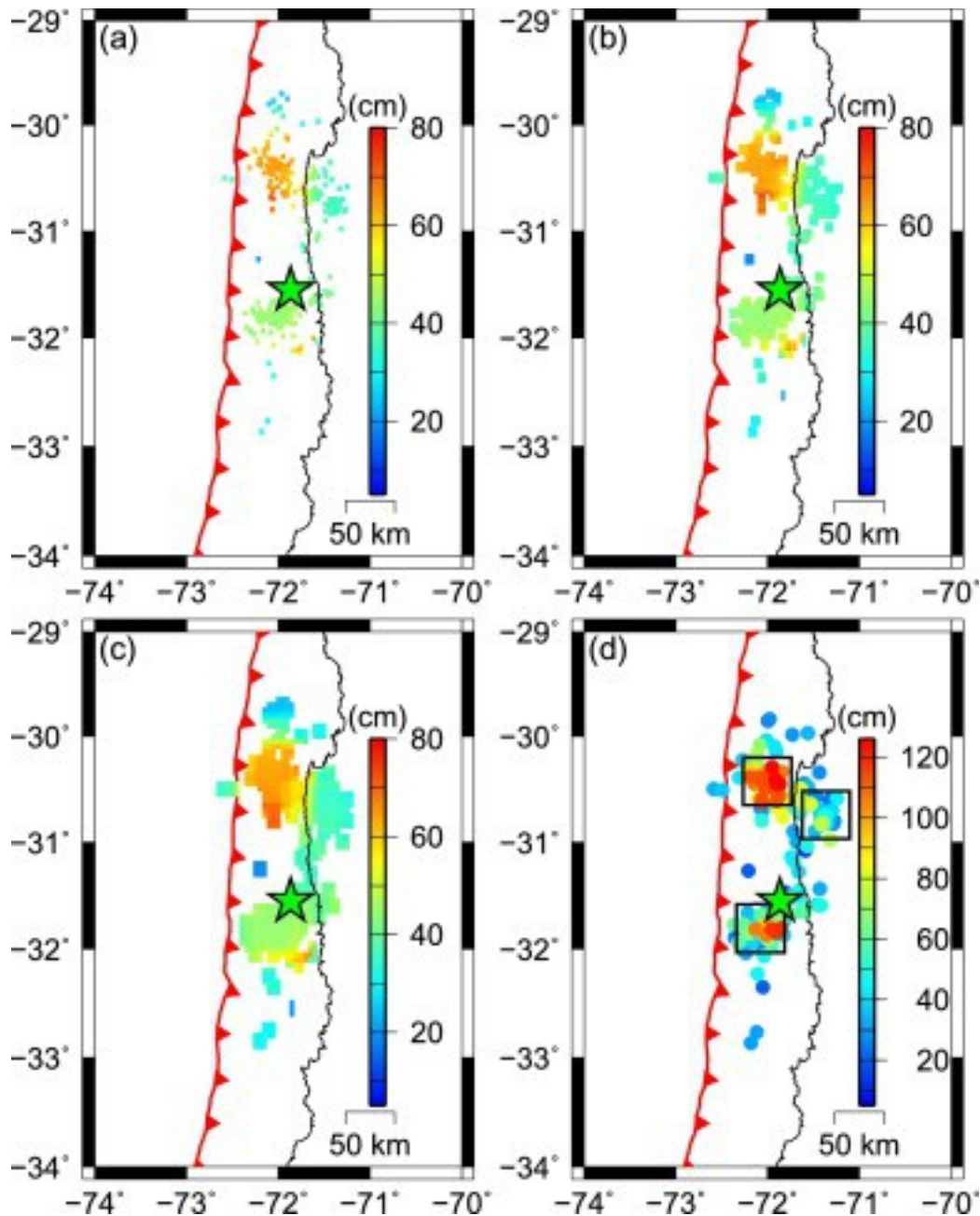
1. [Download high-res image \(1MB\)](#)
2. [Download full-size image](#)

Fig. 4. (a) Events near the trench (to the west of the red line) within one month after the Mw 8.4 mainshock. The red dots denote the 10 [repeaters](#) during this time period. The available [focal mechanisms](#) of some events posted at NEIC or GEOFON are shown. The red line indicates the profile (marked distances in km) where events are projected in (b) and (c), which show the spatio-temporal pattern of [aftershocks](#) and repeaters within the first 30 days and 2 days after the Mw 8.4 mainshock, respectively. Note that the first event of the whole sequence is a M 4.6 event with projected distance 0 km, shown as a

blue star in (a). The dashed line in (c) depicts the possible northward migration in the first several hours. (For interpretation of the references to color in this figure legend, the reader is referred to the web version of this article.)

4. Early afterslip model from repeating earthquakes, GPS and InSAR data

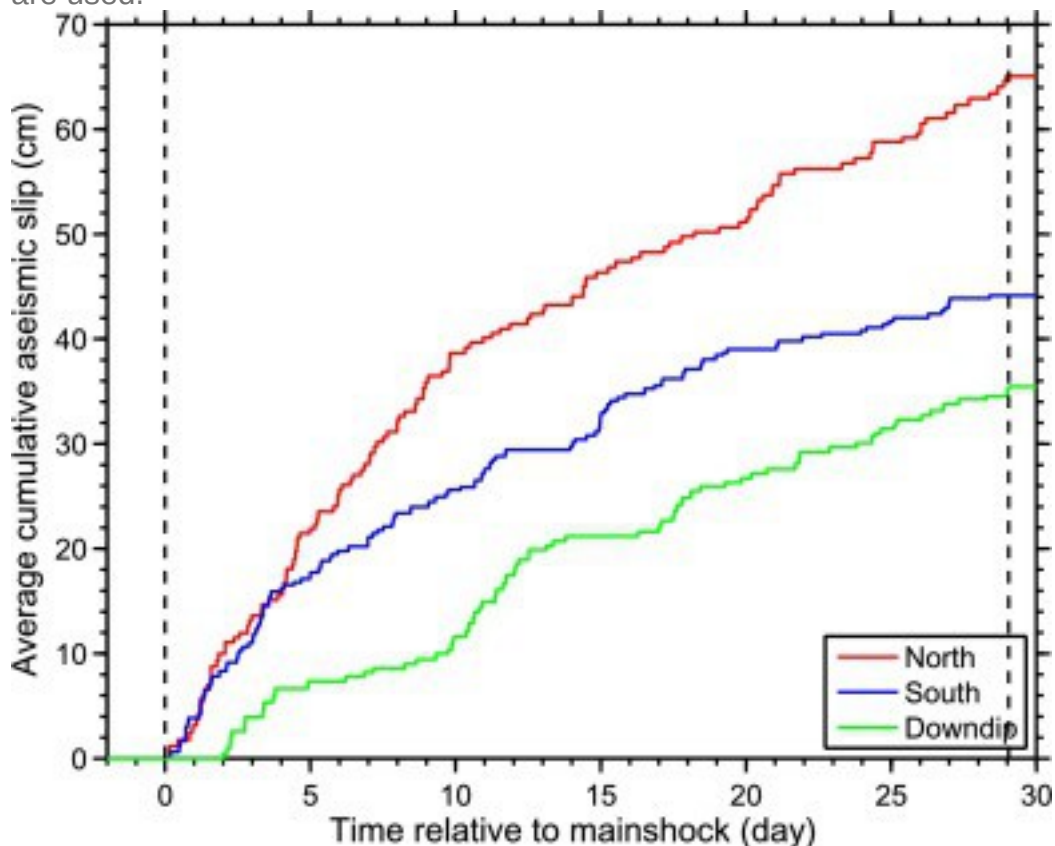
We first estimate the early postseismic slip on the [subduction](#) thrust from the repeating [earthquake](#) data. We exclude burst-type [repeater](#) sequences spanning time intervals of less than 7 days, which may not reflect creep on the [plate boundary](#) ([Templeton et al., 2008](#)). We use the empirical relation introduced by [Nadeau and Johnson \(1998\)](#) to convert the [seismic moment](#) of repeating earthquakes into an estimate of corresponding aseismic-slip increments on the surrounding fault. We apply this aseismic slip estimate to patches of varying sizes around the repeater sequences. Assuming a crustal [shear modulus](#) of 30 GPa, the aseismic moment release estimated from the repeaters is in the range of Mw 7.16–7.51, depending on the prescribed [patch size](#) ([Fig. 5](#)). Note that the total amount of seismic moment of repeaters within the same period is 7.07×10^{17} Nm (Mw 5.83), significantly smaller than the estimated aseismic moment. Because the repeaters are only capable of estimating aseismic slip at positions where small [asperities](#) are available, this estimate may not fully illuminate the spatial extent of afterslip. [Fig. 6](#) shows the different time series of repeater-inferred afterslip in the northern, southern and downdip parts of the mainshock rupture area ([Fig. 5d](#)). Generally the afterslip rate is highest immediately after the mainshock, followed by a decrease with time. The northern patch accumulates the largest afterslip compared to the southern and downdip patches. The inferred afterslip rate fluctuates during the study period, which could reflect the non-steady expansion of the afterslip zone and accelerations associated with large [aftershocks](#). The afterslip series in the northern and southern patch can be well fitted by the afterslip model ([Fig. S8](#), [Marone, 1998](#)).



1. [Download high-res image \(422KB\)](#)
2. [Download full-size image](#)

Fig. 5. Estimated afterslip distribution from repeating [earthquakes](#) during the first month after the mainshock in (a) $0.05^\circ \times 0.05^\circ$ bins (moment $6.94e+19$ N m, Mw 7.16), (b) $0.1^\circ \times 0.1^\circ$ bins ($1.57e + 20$ N m, Mw 7.40) and (c) $0.15^\circ \times 0.15^\circ$ bins ($2.34e + 20$ N m, Mw 7.51). The afterslip value is averaged over a $0.5^\circ \times 0.5^\circ$ grid centered at each moving window. (d) shows the individual repeating earthquakes colored by the cumulative slip during one month after the mainshock. The three boxes ($50 \text{ km} \times 50 \text{ km}$) in (d) show the northern, southern and downdip regions from estimating afterslip time

series in [Fig. 6](#). Only the [repeater](#) sequences that span a time interval of over 7 days are used.

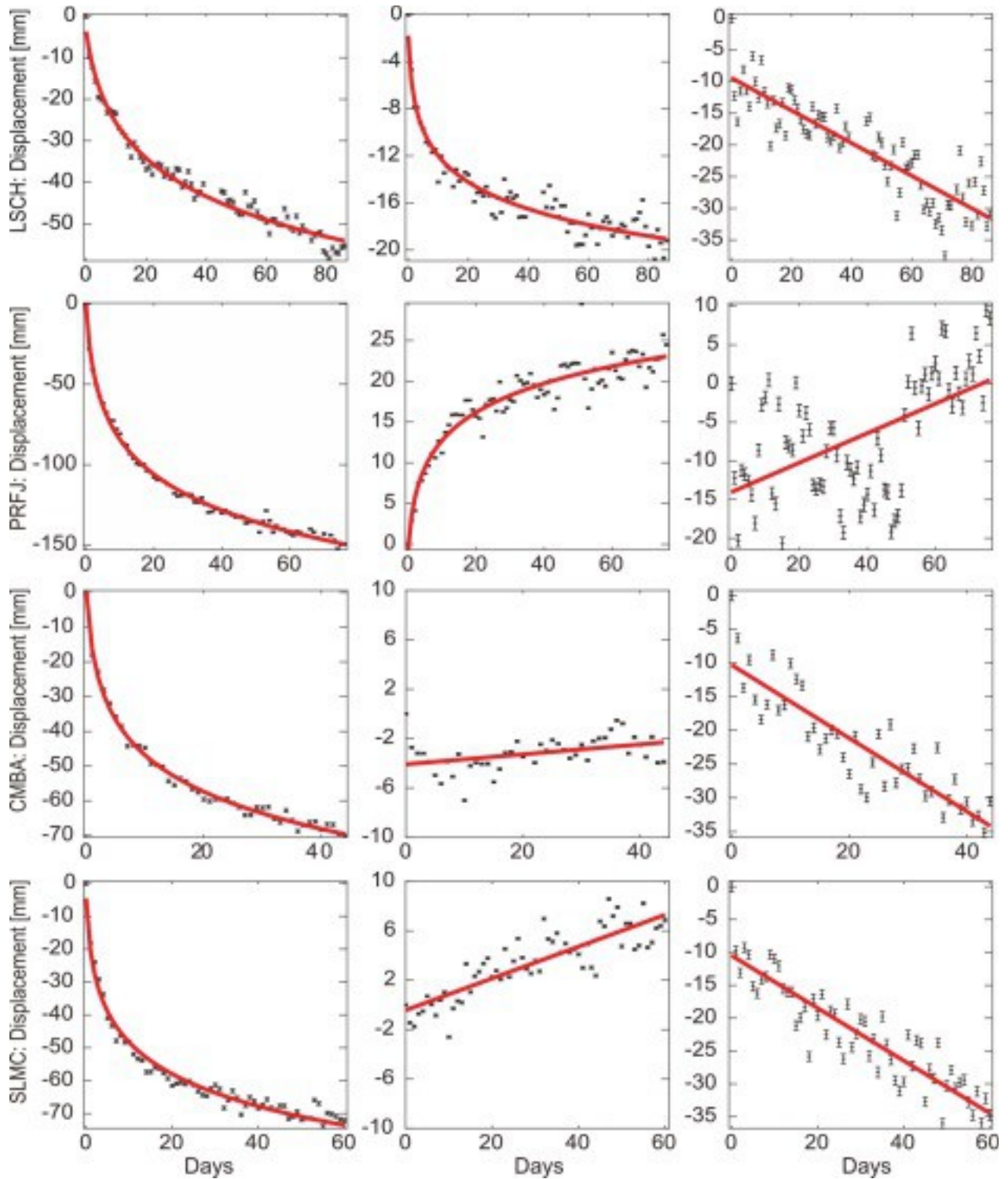


1. [Download high-res image \(184KB\)](#)
2. [Download full-size image](#)

Fig. 6. The average cumulative aseismic slip inferred from the [repeaters](#) within the northern patch (red curve) and the southern patch (blue curve) and downdip patch (green curve). The curves are averaged between different repeater sequences within the three boxes in [Fig. 5d](#). The two dashed vertical lines mark the period when the catalog is improved by [matched-filter](#) analysis. (For interpretation of the references to color in this figure legend, the reader is referred to the web version of this article.)

We further perform an afterslip inversion from both [GPS](#) and InSAR observations. The GPS time series of motions with respect to stable South America are from continuously operating stations in the region processed with the Bernese GPS processing software at the CSN ([Ruiz et al., 2016](#)). The post-seismic GPS time series in the east, north, and vertical directions for four selected stations are shown in [Fig. 7](#). Significant westward to west-northwestward post-seismic displacements of ~ 150 mm are observed at station PRFJ during the first 70 days after the main-shock. The eastward displacements can be well fitted with a logarithmic function. This function can also fit the northward motion at which the stations are located closer to the [epicenter](#). The linear function, however,

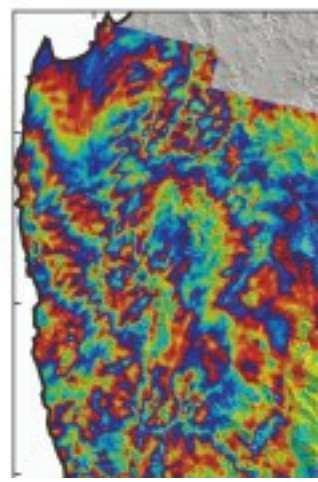
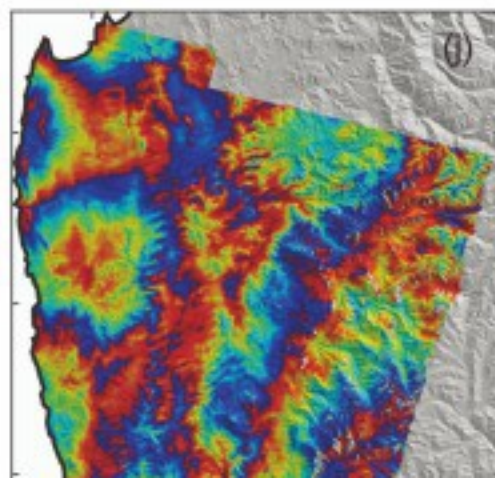
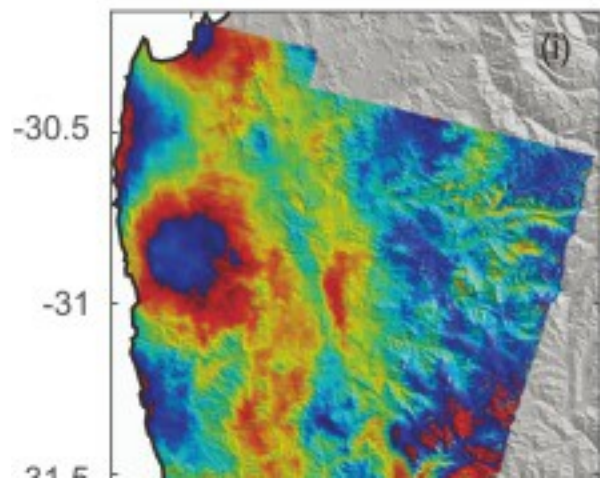
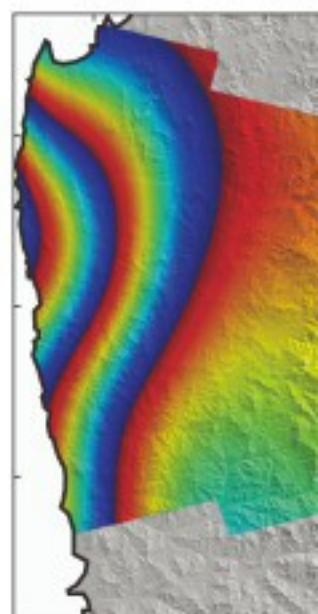
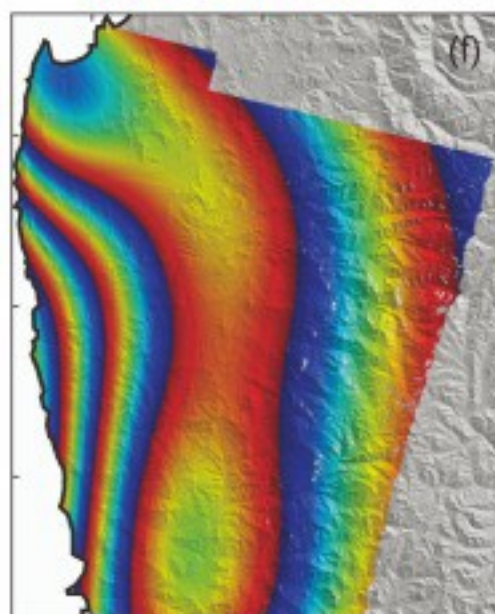
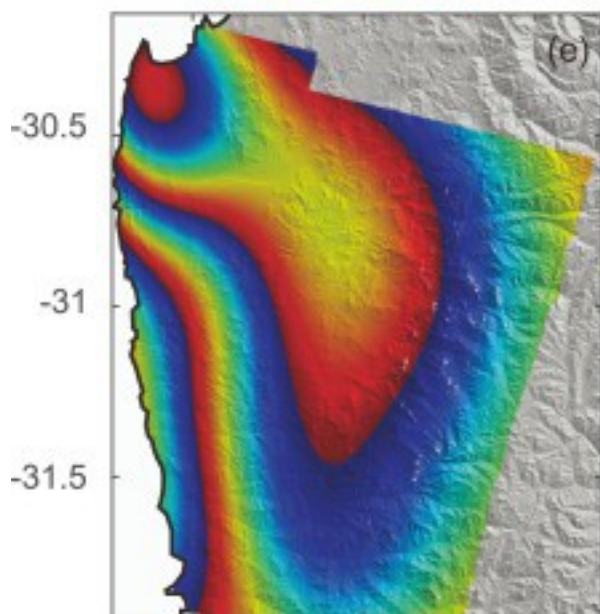
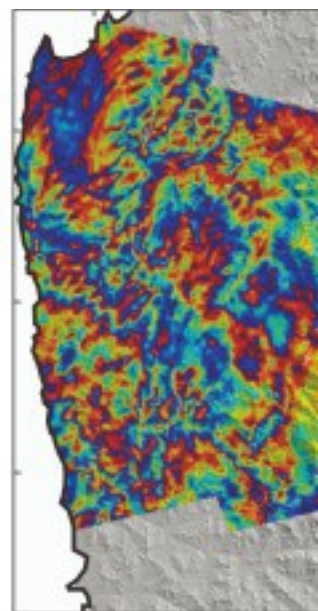
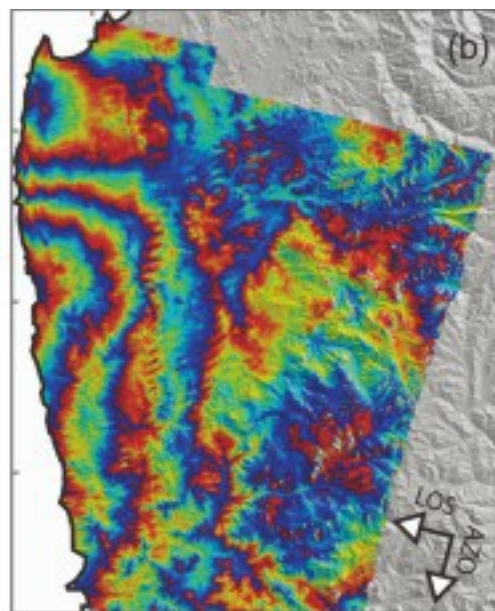
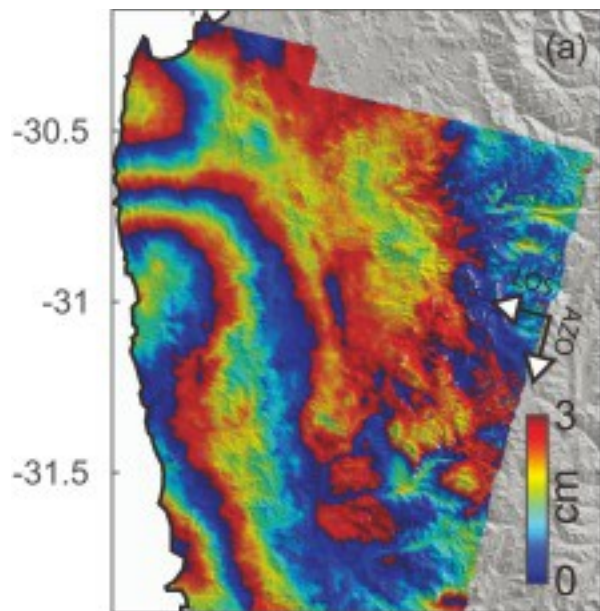
seems to fit the data better in some components ([Fig. 7](#)), which needs to be further checked with longer data. The Sentinel-1A [SAR](#) data are in the Terrain Observation by Progressive Scans (TOPS) mode ([Salvi et al., 2012](#)). In this mode, the antenna sweeping in the [azimuth](#) direction can cause strong Doppler [centroid](#) variation introducing steep azimuth phase ramps across the [interferogram](#). To remove these phase discontinuities, the spectral diversity method is used after applying the intensity [cross correlation](#) between the master and slave images. We process the data with the GAMMA software and use the [Shuttle Radar Topography Mission](#) (SRTM) 3 arc/second DEM ([Farr et al., 2007](#)) to simulate and eliminate the contribution of topography to the measured phase changes. We multilook and filter the interferograms to mitigate noise ([Goldstein and Werner, 1998](#)). Finally, we unwrap the interferograms using the minimum cost flow (MCF) method ([Chen and Zebker, 2000](#)) and geocode them into the WGS84 [coordinate system](#). We generate two interferograms from three Sentinel-1A SAR images collected along the descending orbit ([Figs. 8a and 8b](#)) and two interferograms from three ascending-orbit acquisitions ([Figs. 8c and 8d](#)). [Figs. 8a and 8c](#) show postseismic ground deformation for a period of 24 days starting from one day (descending) and three days (ascending) after the mainshock, respectively, [Figs. 8b and 8d](#) show postseismic ground deformation spanning 48 days. The interferograms from the descending orbit have less noise, possibly because they were acquired in the early morning, while the ascending orbit acquisitions were obtained in the late afternoon leading to more atmospheric noise. The earlier interferogram ([Fig. 8a](#)) shows ~2 fringes of surface displacement from September 17 to October 11 (i.e., ~6 cm in the radar [line-of sight](#) (LOS)) near the coastline at 31°S, while the interferogram from September 17 to November 4 ([Fig. 8b](#)) shows ~4 fringes (~12 cm in LOS). The interferograms from the ascending orbit are contaminated by [atmospheric effects](#), but the 48-day interferogram ([Fig. 8d](#)) shows ~2 fringes of apparent surface displacement (i.e., ~6 cm in LOS).



1. [Download high-res image \(477KB\)](#)
2. [Download full-size image](#)

Fig. 7. Post-seismic [GPS](#) time series at station LSCH (top row), PRFJ (second row), CMBA (third row) and SLMC (bottom row). The scattered points show the [temporal variations](#) found in the east component (first column), north component (second column)

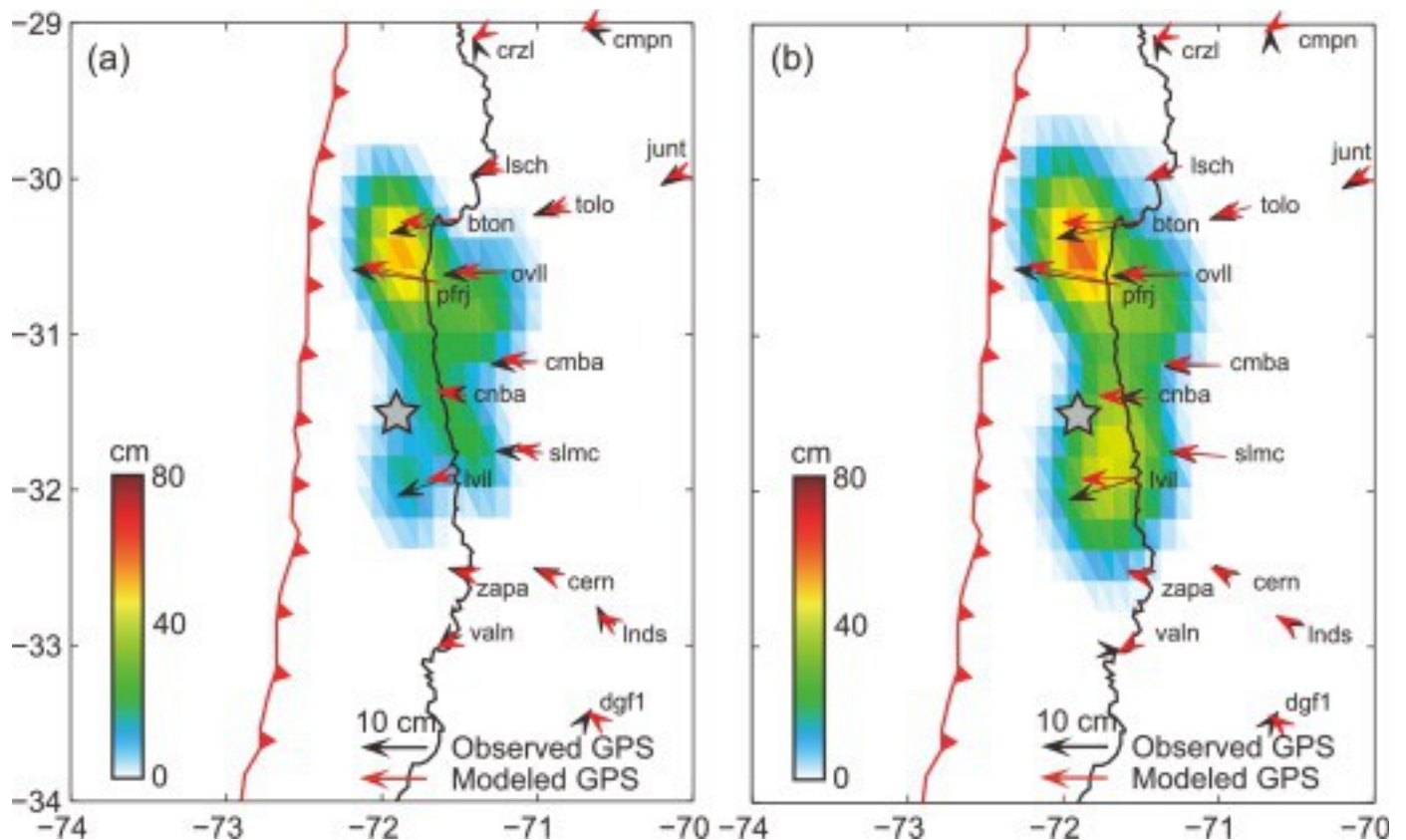
and vertical component (third column). The thick solid red lines show the least-squares fit with a logarithmic or linear function. (For interpretation of the references to color in this figure legend, the reader is referred to the web version of this article.)



1. [Download high-res image \(3MB\)](#)
2. [Download full-size image](#)

Fig. 8. Postseismic InSAR data and [line-of-sight](#) displacements from modeled afterslip. One fringe corresponds to 3 cm of line-of-sight (LOS) displacement. (a–b) Observed [interferograms](#) from the descending orbit spanning 17 Sep. and 11 Oct. and 17 Sep. and 4 Nov., respectively. (c–d) Observed interferograms from the ascending orbit spanning 19 Sep. and 13 Oct. and 19 Sep. and 6 Nov., respectively. (e–h) model predictions of (a–d), (i–l) residuals.

We jointly invert the postseismic GPS data from 17 GPS stations and the unwrapped interferograms from both ascending and descending orbits using a triangular dislocation model in a homogeneous, isotropic, elastic half-space ([Nikkhoo and Walter, 2015](#)) with [Poisson's ratio](#) and shear modulus of 0.25 and 30 GPa, respectively. We adapt the [fault geometry](#) from SLAB 1.0 ([Hayes et al., 2012](#)), which is publicly available from the USGS website (<http://earthquake.usgs.gov/data/slab/>). In the inversion, we only invert for the [fault thrust](#) slip by fixing the rake angle to be 90°. To prevent oscillatory solutions, the inversion is regularized with positivity and smoothness constraints. In general, slip increases with time and the slip pattern is spatially stable over time ([Fig. 9](#)). The position of the postseismic slip maximum is located north of peak coseismic slip. In the first ~24 days after the mainshock, the maximum slip magnitude is 53 cm ([Fig. 9a](#)), and the moment release is 2.3×10^{20} Nm corresponding to Mw 7.5. The rms misfit is 1.6 cm. In comparison, during the first ~50 days after the mainshock, the maximum slip increases to 60 cm north of the epicenter, and a zone of less slip of 45 cm is located south of the epicenter ([Fig. 9b](#)). The 50-day moment release is 2.76×10^{20} Nm corresponding to Mw 7.56. The rms misfit is 1.7 cm. The location of afterslip from the geodetic inversion is generally consistent with the location of repeaters ([Fig. S9](#)). The cumulative afterslip from the geodetic inversion is generally close to or smaller than the repeater-inferred cumulative afterslip, with the largest difference observed to the south of the mainshock ([Fig. S9](#)). This may be due to data uncertainties, smoothing in the geodetic inversion, assumptions regarding elastic [earth structure](#) and fault geometry or the uncertainty of the empirical relation used to convert repeater moments to aseismic slip. Both the seismic and [geodetic data](#) sets show that there are two predominant patches of afterslip to the north and south of the mainshock rupture ([Fig. 9](#)). The northern patch at ~30.5°S is characterized by larger cumulative aseismic slip than the southern patch during the first month ([Figs. 5 and 9a](#)). The afterslip also extends downdip of the coseismic rupture zone ([Fig. 9](#)).



1. [Download high-res image \(339KB\)](#)
2. [Download full-size image](#)

Fig. 9. Afterslip distribution estimated from the joint inversion of InSAR and [GPS](#) data (a) between 17 September and 13 October and (b) 17 September and 6 November, respectively. Black and red arrows show observed and modeled GPS horizontal displacements. (For interpretation of the references to color in this figure legend, the reader is referred to the web version of this article.)

5. Discussion and conclusions

5.1. The spatio-temporal evolution of early aftershock sequence

In our study, the observed along-strike expansion of early [aftershocks](#) within the first day raises the question of aftershock triggering mechanisms. Both static and dynamic triggering may play an important role in the aftershock zone surrounding the mainshock rupture ([Felzer and Brodsky, 2006](#), [Gomberg et al., 2003](#), [van der Elst and Brodsky, 2010](#)). In addition, aseismic afterslip was found to be the driving mechanism of aftershock zone expansion of other events (e.g., [Perfettini and Avouac, 2004](#), [Hsu et al., 2006](#)), including the 2004 Mw 6.0 Parkfield [earthquake](#) ([Peng and Zhao, 2009](#)) and the 2011 Mw 9.0 Tohoku-Oki earthquake ([Lengliné et al., 2012](#)). For the 2015 Illapel

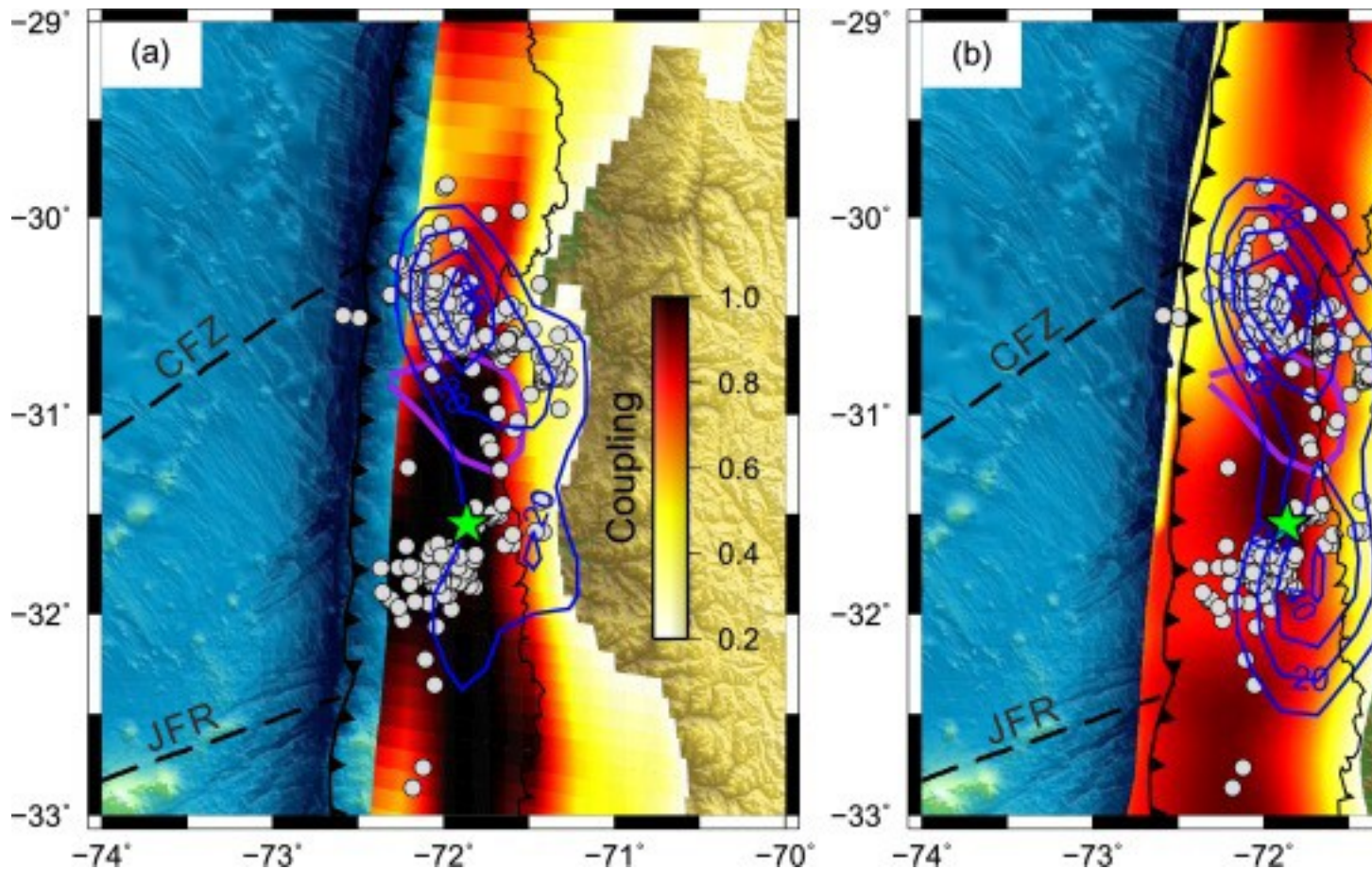
earthquake, [Tilmann et al. \(2016\)](#) found that most of the thrust-faulting aftershocks are distributed in areas of positive Coulomb stress change, suggesting the importance of static triggering and/or triggering by afterslip driven by the stress increase. [Lange et al. \(2016\)](#) found faster along-strike migration of aftershocks to the south (5 km/day) than to the north (2.5 km/day) within the first day. Our results show that the aftershocks accompanied by [repeaters](#) suddenly advanced to the south at ~14 h after the mainshock while they steadily migrated to the north. Repeating earthquakes, indicative of recurrent ruptures of the same fault patch, are primarily induced by surrounding aseismic slip ([Nadeau and Johnson, 1998](#)). In our study, the collocation of repeaters and afterslip inverted from independent [geodetic data](#) supports the viewpoint that repeaters are mainly driven by afterslip on the megathrust. The sudden southward expansion may be explained by propagating afterslip encountering a relatively strong [asperity](#), which finally breaks ~14 h later in an Mw 6.0 event due to the continuous loading by afterslip. A similar sudden expansion is observed in the aftershock zone of the 2004 Mw 6.0 Parkfield earthquake migrating towards the locked portion of the [San Andreas fault](#) ([Peng and Zhao, 2009](#)) and the aftershock zone of the 2007 Mw 6.7 Noto-Hanto earthquake when encountering a complex segmented fault zone ([Kato and Obara, 2014](#)). In contrast, the relatively continuous northward expansion within the first day may be related to the wide distribution of areas with velocity-strengthening fault properties to the north (will be discussed in section [5.2](#)). This suggests the spatial heterogeneity of fault frictional properties on the fault and/or complex structures such as subducted [seamounts](#) to the south of the Illapel rupture (e.g., [Laursen and Normark, 2002](#), [Yáñez et al., 2001](#)) may control the pattern of aftershock expansion. Overall, our results suggest that stress-driven afterslip is an important mechanism for the triggering and early expansion of aftershocks of the Illapel event in addition to other possible physical processes, such as stress transfer or poroelastic effects.

In addition, the observation of a large cluster of triggered events near the trench, which initiated with a delay of ~3.5 h, is intriguing. They may occur within the oceanic plate, on the shallow plate interface and/or within the hanging wall of the megathrust. Some of these events are normal-faulting earthquakes, consistent with increased tension in the outer rise ([Tilmann et al., 2016](#)). A large number of triggered outer-rise events is often seen as an indicator of large coseismic slip near the trench ([Christensen and Ruff, 1983](#), [Lay et al., 2009](#)). This is consistent with significant slip reaching the trench revealed by the back-projection and finite-fault inversion studies of the Illapel earthquake (e.g., [Melgar et al., 2016](#), [Tilmann et al., 2016](#)). The delayed initiation of the sequence may indicate that the immediate static stress at the outer rise was not

sufficient to instantly trigger events and that an aseismic process, such as slow slip or [fluid flow](#), was needed to initiate this sequence. This short delay time may also indicate time-dependent earthquake [nucleation](#) processes (e.g., [Dieterich, 1994](#)). Another possible effect is dynamic triggering, which is often observed in triggering events at remote distances by passing [surface waves](#) (e.g., [Hill et al., 1993](#)) but also can promote earthquakes nearby a rupture (e.g., [Kilb et al., 2000](#)). A delayed dynamic triggering response may reflect nonlinear frictional fault properties, fluid migration, and/or aseismic [fault slip](#) ([Hill and Prejean, 2015](#)). Our results suggest that the events near the trench migrate along the trench [axis](#) in the first several hours. This might suggest the existence of aseismic slip and/or fluid flow to cause the delayed triggering and migration of events. Slow slip may be indicated by the five repeater pairs that occurred during the first month following the mainshock ([Fig. 4a](#)), but due to the lack of more and precisely located repeater sequences and geodetic constraints, it is uncertain if a slow slip component occurs on the outer-rise faults.

5.2. The early afterslip distribution of the 2015 Illapel event

The afterslip distribution has important implications for the segmentation of the plate interface and how the stress increase induced by the mainshock is released. [Fig. 10](#) shows a comparison of repeating earthquakes and afterslip inverted from geodetic data with the coseismic slip model ([An and Meng, 2016](#)) and coupling models inferred from interseismic surface deformation ([Métois et al., 2014](#), [Tilmann et al., 2016](#)). We observe a first-order spatial anti-correlation between the afterslip delineated by both repeaters and geodetic inversion and the area of large coseismic slip. This is consistent with observations of the 2011 Tohoku-Oki earthquake ([Ozawa et al., 2011](#)), the 2014 Iquique earthquake ([Meng et al., 2015](#)) and the 2007 Pisco earthquake along the central Peru megathrust ([Perfettini et al., 2010](#)). The large coseismic slip is collocated with an area of strong interseismic coupling. Extensive afterslip may be expected in areas of low interseismic coupling, where static coseismic stress increases can accelerate aseismic slip (e.g., [Kato and Igarashi, 2012](#), [Uchida and Matsuzawa, 2013](#)).



1. [Download high-res image \(1MB\)](#)
2. [Download full-size image](#)

Fig. 10. First one-month repeating [earthquake](#) distributions (gray circles) and afterslip (blue contours in cm) from geodetic inversion between (a) 17 September and 13 October and (b) 17 September and 6 November. The plate coupling model in (a) is from [Métois et al. \(2014\)](#), which uses [GPS](#) data from 2004 to 2012; the model in (b) is from [Tilmann et al. \(2016\)](#), reflecting coupling before the 2010 Maule earthquake. The purple curve denotes 5 m coseismic slip contour lines from [An and Meng \(2016\)](#). CFZ denotes the Challenger [Fracture Zone](#) and JFR indicates the Juan-Fernández Ridge. (For interpretation of the references to color in this figure legend, the reader is referred to the web version of this article.)

To the south of the mainshock rupture area, the observation of afterslip may suggest the changes in [pore fluid pressure fields](#) induced by the coseismic rupture or the existence of a relatively weak coupling area. The latter is supported by the coupling model by [Tilmann et al. \(2016\)](#), which shows a transition from strong to weak coupling southward of the Illapel [epicenter](#) ([Fig. 10b](#)). This supports a scenario in which the mainshock rupture initiates along the edge of the locked patch where the concentration

of pre-earthquake loading stress is high. This relatively weakly coupled, velocity strengthening area may have inhibited the southward rupture propagation, which is consistent with the northward unilateral propagation in the initial stage of rupture (e.g., [Melgar et al., 2016](#)). To the north of the mainshock rupture, both repeaters and geodetic inversion indicate larger cumulative afterslip in a wider area than the south and downdip. This is consistent with the afterslip distribution obtained by [GPS](#) and InSAR inversion in a recent study ([Barnhart et al., 2016](#)). This can be well explained by the wide low coupling zone to the north of the rupture zone at $\sim 30.5^\circ\text{S}$, which correlates well with the location of the CFZ ([Fig. 10](#), [Ruiz et al., 2016](#)). The different afterslip behavior to the north and south of the rupture zone may be explained by the different size and/or mechanical behavior of the low-coupling zones. The low-coupling zones to the north and south of the Illapel rupture area may be explained by the subducting [fracture zones](#) or ridges, which can reduce the coupling of the plate interface by inducing [fracture networks](#) ([Wang and Bilek, 2011](#), [Lange et al., 2016](#)). Our results suggest that coseismic stress increases lead to rapid afterslip to make up the previously accumulated slip deficit on the along-strike and downdip sections of the mainshock rupture. But it is important to keep in mind that despite the evidence of postseismic slow slip on these zones, future events' dynamic slip may still break through such uncoupled fault sections if rapid shear heating of pore fluids is involved ([Noda and Lapusta, 2013](#)). The afterslip moment in the first ~ 24 days as inferred from the geodetic measurements is $2.3 \times 10^{20} \text{Nm}$ equivalent to $M_w \sim 7.51$. The cumulative [seismic moment](#) release of aftershocks ($M_w \geq 4$) during the corresponding time period amounts to $5.21 \times 10^{19} \text{Nm}$ ($M_w \sim 7.08$), indicating that a significant portion ($\sim 77\%$) of the slip was released by aseismic creep. Note that the calculation of seismic moment excludes the first ~ 11 -h of aftershocks not spanned by the InSAR data, the total seismic moment released during this period is significant ($4.18 \times 10^{20} \text{Nm}$, $M_w \sim 7.68$). The afterslip expansion in the along-strike direction may lead to enhanced stress loading of the adjacent locked patches of the 1906 M 8.4 earthquake to the south and the 1922 M 8.4 earthquake to the north. This stresses the importance of monitoring of microseismicity and slow slip around these locked zones.

Acknowledgments

We appreciate valuable comments from Diego Melgar and discussions with Zhouchuan Huang. The IRIS (www.iris.edu) data centers provided access to broadband [seismograms](#) used in this study. We thank the Centro Sismológico Nacional for providing seismic and [GPS](#) data from their networks. Sentinel-

1A [interferograms](#) used in our analysis are derived from Copernicus data, subject to [ESA](#) use and distribution conditions. This work used computational and storage services associated with the Hoffman2 Shared Cluster provided by UCLA Institute for Digital Research and Education's Research Technology Group. This study is supported by the Knopoff foundation, NSF [EAR-1614609](#) and Special [Earthquake](#) Early Warning project [16A43ZX236](#) of China Earthquake Agency.

Appendix A. Supplementary material

The following is the Supplementary material related to this article.

[Download Word document \(3MB\)](#)[Help with docx files](#)

Supplementary material. Supporting information includes 1 table (Table S1) and 9 figures (Figs. S1–S9).

References

[An and Meng, 2016](#)

C. An, L. Meng **Application of array backprojection to tsunami prediction and early warning**
Geophys. Res. Lett., 43 (2016), [10.1002/2016GL068786](#)

[Angermann et al., 1999](#)

D. Angermann, J. Klotz, C. Reigber **Space-geodetic estimation of the Nazca-South America Euler vector**

Earth Planet. Sci. Lett., 171 (3) (1999), pp. 329-334

[Article](#)[Download PDF](#)[View Record in Scopus](#)

[Barnhart et al., 2016](#)

W.D. Barnhart, J.R. Murray, R.W. Briggs, F. Gomez, C.P.J. Miles, J. Svare, S. Riquelme, B.J. Streissler **Coseismic slip and early afterslip of the 2015 Illapel, Chile, earthquake: implications for frictional heterogeneity and coastal uplift**

J. Geophys. Res., Solid Earth, 121 (2016), [10.1002/2016JB013124](#)

[Chen and Zebker, 2000](#)

C.W. Chen, H.A. Zebker **Network approaches to two-dimensional phase unwrapping: intractability and two new algorithms**

J. Opt. Soc. Am., 17 (2000), pp. 401-414

[CrossRef](#)[View Record in Scopus](#)

[Christensen and Ruff, 1983](#)

D.H. Christensen, L.J. Ruff **Outer-rise earthquakes and seismic coupling**

Geophys. Res. Lett., 10 (8) (1983), pp. 697-700

[CrossRef](#)[View Record in Scopus](#)

[Dieterich, 1994](#)

J. Dieterich **A constitutive law for rate of earthquake production and its application to earthquake clustering**

J. Geophys. Res., 99 (B2) (1994), pp. 2601-2618, [10.1029/93JB02581](https://doi.org/10.1029/93JB02581)
[CrossRefView Record in Scopus](#)

[Farr et al., 2007](#)

T.G. Farr, *et al.* **The shuttle radar topography mission**
Rev. Geophys., 45 (2007), Article RG2004, [10.1029/2005RG000183](https://doi.org/10.1029/2005RG000183)

[Felzer and Brodsky, 2006](#)

K.R. Felzer, E.E. Brodsky **Decay of aftershock density with distance indicates triggering by dynamic stress**

Nature, 441 (7094) (2006), pp. 735-738

[CrossRefView Record in Scopus](#)

[Goldstein and Werner, 1998](#)

R.M. Goldstein, C.L. Werner **Radar interferogram filtering for geophysical applications**
Geophys. Res. Lett., 25 (1998), pp. 4035-4038

[CrossRefView Record in Scopus](#)

[Gomberg et al., 2003](#)

J. Gomberg, P. Bodin, P.A. Reasenber **Observing earthquakes triggered in the near field by dynamic deformations**

Bull. Seismol. Soc. Am., 93 (1) (2003), pp. 118-138

[CrossRefView Record in Scopus](#)

[Hayes et al., 2012](#)

G.P. Hayes, D.J. Wald, R.L. Johnson **Slab1.0: a three-dimensional model of global subduction zone geometries**

J. Geophys. Res., 117 (2012), Article B01302, [10.1029/2011JB008524](https://doi.org/10.1029/2011JB008524)

[Heidarzadeh et al., 2016](#)

M. Heidarzadeh, S. Murotani, K. Satake, T. Ishibe, A.R. Gusman **Source model of the 16 September 2015 Illapel, Chile, Mw 8.4 earthquake based on teleseismic and tsunami data**

Geophys. Res. Lett., 43 (2016), pp. 643-650, [10.1002/2015GL067297](https://doi.org/10.1002/2015GL067297)

[CrossRefView Record in Scopus](#)

[Hill and Prejean, 2015](#)

D.P. Hill, S.G. Prejean **Dynamic triggering**

G. Schubert (Ed.), Treatise on Geophysics (2nd edition), Elsevier, Oxford (2015), pp. 273-304

[ArticleDownload PDFView Record in Scopus](#)

[H](#)
[i](#)
[!](#)
[!](#)

D.P. Hill, *et al.* **Seismicity remotely triggered by the magnitude 7.3 Landers, California, earthquake**

Science, 260 (5114) (1993), pp. 1617-1623

[View Record in Scopus](#)

[Hsu et al., 2006](#)

Y.J. Hsu, M. Simons, J.P. Avouac, J. Galetzka, K. Sieh, M. Chlieh, D. Natawidjaja, L. Prawirodirdjo, Y. Bock **Frictional afterslip following the 2005 Nias-Simeulue earthquake, Sumatra**

Science, 312 (5782) (2006), pp. 1921-1926

[CrossRefView Record in Scopus](#)

[Igarashi et al., 2003](#)

T. Igarashi, T. Matsuzawa, A. Hasegawa **Repeating earthquakes and interplate aseismic slip in the northeastern Japan subduction zone**

J. Geophys. Res., 108 (2003), p. 2249

[Kato and Igarashi, 2003](#)

A. Kato, T. Igarashi **Regional extent of the large coseismic slip zone of the 2011 Mw 9.0 Tohoku-Oki earthquake delineated by on-fault aftershocks**

Geophys. Res. Lett., 39 (2012), Article L15301, [10.1029/2012GL052220](#)

[Kato and Obara, 2012](#)

A. Kato, K. Obara **Step-like migration of early aftershocks following the 2007 Mw 6.7 Noto-Hanto earthquake, Japan**

Geophys. Res. Lett., 41 (2014), pp. 3864-3869, [10.1002/2014GL060427](#)

[CrossRefView Record in Scopus](#)

[Kato et al., 2012](#)

A. Kato, K. Obara, T. Igarashi, H. Tsuruoka, S. Nakagawa, N. Hirata **Propagation of slow slip leading up to the 2011 Mw 9.0 Tohoku-Oki earthquake**

Science, 335 (2012), pp. 705-708

[CrossRefView Record in Scopus](#)

[Kilb et al., 2000](#)

D. Kilb, J. Gomberg, P. Bodin **Triggering of earthquake aftershocks by dynamic stresses**

Nature, 408 (6812) (2000), pp. 570-574

[View Record in Scopus](#)

[Lange et al., 2016](#)

D. Lange, J. Geersen, S. Barrientos, M. Moreno, I. Grevemeyer, E. Contreras-Reyes, H. Kopp **Aftershock seismicity and tectonic setting of the 16 September 2015 Mw 8.3 Illapel earthquake, Central Chile**

Geophys. J. Int., 206 (2016), pp. 1424-1430, Article ggw218

[Laursen and Normark, 2002](#)

J. Laursen, W.R. Normark **Late Quaternary evolution of the San Antonio Submarine Canyon in the central Chile forearc (~33S)**

Mar. Geol., 188 (3) (2002), pp. 365-390

[ArticleDownload PDFView Record in Scopus](#)

[Lay et al., 2009](#)

T. Lay, H. Kanamori, C.J. Ammon, A.R. Hutko, K. Furlong, L. Rivera **The 2006–2007 Kuril Islands great earthquake sequence**

J. Geophys. Res., 114 (2009), Article B11308, [10.1029/2008JB006280](#)

[Lengliné et al., 2012](#)

O. Lengliné, B. Enescu, Z. Peng, K. Shiomi **Decay and expansion of the early aftershock activity following the 2011, Mw 9.0 Tohoku earthquake**

Geophys. Res. Lett., 39 (2012), Article L18309, [10.1029/2012GL052797](#)

[Marone, 1998](#)

C. Marone **Laboratory-derived friction laws and their application to seismic faulting**

Annu. Rev. Earth Planet. Sci., 26 (1998), pp. 643-696

[CrossRefView Record in Scopus](#)

[Melgar et al., 2016](#)

D. Melgar, W. Fan, S. Riquelme, J. Geng, C. Liang, M. Fuentes, G. Vargas, R.M. Allen, P.M. Shearer, E.J. Fielding **Slip segmentation and slow rupture to the trench during the 2015, Mw8.3 Illapel, Chile earthquake**

Geophys. Res. Lett., 43 (2016), pp. 961-966, [10.1002/2015GL067369](#)

[CrossRefView Record in Scopus](#)

[Meng et al., 2014](#)

L. Meng, H. Huang, R. Bürgmann, J.P. Ampuero, A. Strader **Dual megathrust slip behaviors of the 2014 Iquique earthquake sequence**

Earth Planet. Sci. Lett., 411 (2015), pp. 177-187

[ArticleDownload PDFView Record in Scopus](#)

[Métois et al., 2015](#)

M. Métois, A. Socquet, C. Vigny **Interseismic coupling, segmentation and mechanical behavior of the central Chile subduction zone**

J. Geophys. Res., 117 (2012), Article B03406, [10.1029/2011JB008736](#)

[Métois et al., 2012](#)

M. Métois, C. Vigny, A. Socquet, A. Delorme, S. Morvan, I. Ortega, C.-M. Valderas-Bermejo **GPS-derived interseismic coupling on the subduction and seismic hazards in the Atacama region, Chile**

Geophys. J. Int., 196 (2) (2014), pp. 644-655, [10.1093/gji/ggt418](#)

[CrossRef](#)

[Nadeau and Johnson, 1998](#)

R.M. Nadeau, L.R. Johnson **Seismological studies at Parkfield VI: moment re-lease rates and estimates of source parameters for small repeating earthquakes**

Bull. Seismol. Soc. Am., 88 (1998), pp. 790-814

[View Record in Scopus](#)

[Nadeau and McEvilly, 1999](#)

R.M. Nadeau, T.V. McEvilly **Fault slip rates at depth from recurrence intervals of repeating microearthquakes**

Science, 285 (1999), pp. 718-721

[CrossRefView Record in Scopus](#)

[Nikkhoo and Walter, 2015](#)

M. Nikkhoo, T.R. Walter **Triangular dislocation: an analytical, artefact-free solution**

Geophys. J. Int., 2 (2015), pp. 1117-1139, [10.1093/gji/ggv035](#)

[View Record in Scopus](#)

[Noda and Lapusta, 2013](#)

H. Noda, N. Lapusta **Stable creeping fault segments can become destructive as a result of dynamic weakening**

Nature, 493 (7433) (2013), pp. 518-521

[CrossRefView Record in Scopus](#)

[Okuwaki et al., 2016](#)

R. Okuwaki, Y. Yagi, R. Aránguiz, J. González, G. González **Rupture process during the 2015 Illapel, Chile earthquake: zigzag-along-dip rupture episodes**

Pure Appl. Geophys., 173 (2016), pp. 1011-1020, [10.1007/s00024-016-1271-6](#)

[CrossRefView Record in Scopus](#)

[Ozawa et al., 2011](#)

S. Ozawa, T. Nishimura, H. Suito, T. Kobayashi, M. Tobito, T. Imakiire **Coseismic and postseismic slip of the 2011 magnitude-9 Tohoku-Oki earthquake**

Nature, 475 (2011), pp. 373-376, [10.1038/nature10227](https://doi.org/10.1038/nature10227)

[CrossRef](#)

[Peng and Zhao,](#)

Z. Peng, P. Zhao **Migration of early aftershocks following the 2004 Parkfield earthquake**

Nat. Geosci., 2 (2009), pp. 877-881

[CrossRef](#)[View Record in Scopus](#)

[Perfettini and Av](#)

H. Perfettini, J.-P. Avouac **Postseismic relaxation driven by brittle creep: a possible mechanism to reconcile geodetic measurements and the decay rate of aftershocks, application to the Chi-Chi earthquake, Taiwan**

J. Geophys. Res., 109 (2004), Article B02304, [10.1029/2003JB002488](https://doi.org/10.1029/2003JB002488)

[View Record in Scopus](#)

[Perfettini et al., 2](#)

H. Perfettini, J.P. Avouac, H. Tavera, A. Kositsky, J.M. Nocquet, F. Bondoux, P. Soler **Seismic and aseismic slip on the Central Peru megathrust**

Nature, 465 (7294) (2010), pp. 78-81

[CrossRef](#)[View Record in Scopus](#)

[Ruiz et al., 2016](#)

S. Ruiz, E. Klein, F. del

Campo, E. Rivera, P. Poli, M. Métois, C. Vigny, J.C. Baez, G. Vargas, F. Leyton, R. Madariaga, L. Fleitout **The seismic sequence of the 16 September 2015 Mw 8.3 Illapel, Chile, earthquake**

Seismol. Res. Lett., 87 (2016), [10.1785/0220150281](https://doi.org/10.1785/0220150281)

[Salvi et al., 2012](#)

S. Salvi, S. Stramondo, G.J. Funning, A. Ferretti, F. Sarti, A. Mouratidis **The Sentinel-1 mission for the improvement of the scientific understanding and the operational monitoring of the seismic cycle**

Remote Sens. Environ., 120 (2012), pp. 164-174, [10.1016/j.rse.2011.09.029](https://doi.org/10.1016/j.rse.2011.09.029)

[ArticleDownload PDF](#)[View Record in Scopus](#)

[Shirzaei et al., 20](#)

M. Shirzaei, R. Bürgmann, T. Taira **Implications of recent asperity failures and aseismic creep for time-dependent earthquake hazard on the Hayward fault**

Earth Planet. Sci. Lett., 371–372 (2013), pp. 59-66, [10.1016/j.epsl.2013.04.024](https://doi.org/10.1016/j.epsl.2013.04.024)

[ArticleDownload PDF](#)[View Record in Scopus](#)

[Templeton et al.,](#)

D.C. Templeton, R.M. Nadeau, R. Bürgmann **Behavior of repeating earthquake sequences in Central California and the implications for subsurface fault creep**

Bull. Seismol. Soc. Am., 98 (2008), pp. 52-65

[CrossRef](#)[View Record in Scopus](#)

[Tilmann et al., 20](#)

F. Tilmann, *et al.* **The 2015 Illapel earthquake, central Chile: a type case for a characteristic earthquake?**

Geophys. Res. Lett., 43 (2016), pp. 574-583, [10.1002/2015GL066963](https://doi.org/10.1002/2015GL066963)

[CrossRefView Record in Scopus](#)

[Uchida and Mats](#)

N. Uchida, T. Matsuzawa **Pre- and postseismic slow slip surrounding the 2011 Tohoku-oki earthquake rupture**

Earth Planet. Sci. Lett., 374 (2013), pp. 81-91

[ArticleDownload PDFView Record in Scopus](#)

[Uchida et al., 20](#)

N. Uchida, A. Hasegawa, T. Matsuzawa, T. Igarashi **Pre- and postseismic slow slip on the plate boundary off Sanriku, NE Japan associated with three interplate earthquakes as estimated from small repeating earthquake data**

Tectonophysics, 385 (2004), pp. 1-15

[ArticleDownload PDFView Record in Scopus](#)

[van der Elst and](#)

N.J. van der Elst, E.E. Brodsky **Connecting near-field and far-field earthquake triggering to dynamic strain**

J. Geophys. Res., 115 (B07311) (2010), [10.1029/2009JB006681](https://doi.org/10.1029/2009JB006681)

[Wang and Bilek, 2011](#)

K. Wang, S.L. Bilek **Do subducting seamounts generate or stop large earthquakes?**

Geology, 39 (2011), pp. 819-822

[CrossRefView Record in Scopus](#)

[Yáñez et al., 2001](#)

G.A. Yáñez, C.R. Ranero, R. vonHuene, J. Díaz **Magnetic anomaly interpretation across the southern central Andes (32°–34°S): the role of the Juan Fernández Ridge in the late Tertiary evolution of the margin**

J. Geophys. Res., 106 (B4) (2001), pp. 6325-6345, [10.1029/2000JB900337](https://doi.org/10.1029/2000JB900337)

[CrossRefView Record in Scopus](#)

[Yin et al., 2016](#)

J. Yin, H. Yang, H. Yao, H. Weng **Coseismic radiation and stress drop during the 2015 Mw 8.3 Illapel, Chile megathrust earthquake**

Geophys. Res. Lett., 43 (2016), pp. 1520-1528, [10.1002/2015GL067381](https://doi.org/10.1002/2015GL067381)

[CrossRefView Record in Scopus](#)

[Zhang and Wen, 2015](#)

M. Zhang, L. Wen **An effective method for small event detection: Match and locate (M&L)**

Geophys. J. Int., 200 (3) (2015), pp. 1523-1537

[CrossRefView Record in Scopus](#)